Theoretical, experimental, and computational aspects of optical property determination of turbid media by using frequency-domain laser infrared photothermal radiometry

Lena Nicolaides, Yan Chen, and Andreas Mandelis

Photothermal and Optoelectronic Diagnostics Laboratories, Department of Mechanical and Industrial Engineering, University of Toronto, 5 King's College Road, Toronto, Ontario Canada M5S3G8

I. Alex Vitkin

Department of Medical Biophysics, University of Toronto and Ontario Cancer Institute, 610 University Avenue, Toronto, Ontario Canada M5G2M9

Received November 29, 2000; revised manuscript received February 23, 2001; accepted March 12, 2001

In this work, the optical and thermal properties of tissuelike materials are measured by using frequency-domain infrared photothermal radiometry. This technique is better suited for quantitative multiparameter optical measurements than the widely used pulsed-laser photothermal radiometry (PPTR) because of the availability of two independent signal channels, amplitude and phase, and the superior signal-to-noise ratio provided by synchronous lock-in detection. A rigorous three-dimensional (3-D) thermal-wave formulation with a 3-D diffuse and coherent photon-density-wave source is applied to data from model phantoms. The combined theoretical, experimental, and computational methodology shows good promise with regard to its analytical ability to measure optical properties of turbid media uniquely, as compared with PPTR, which exhibits uniqueness problems. From data sets obtained by using calibrated test phantoms, the reduced optical scattering and absorption coefficients were found to be within 20% and 10%, respectively, of the values independently derived by using Mie theory and spectrophotometric measurements.

OCIS codes: 170.4580, 260.3060.

1. INTRODUCTION

Frequency-domain photothermal radiometry (FD-PTR) is a growing technology for the nondestructive evaluation of subsurface features in opaque materials.[1,2] The technique is based on the modulated thermal infrared (blackbody or Planck-radiation) response of a medium, resulting from radiation absorption and nonradiative energy conversion, followed by temperature rise. The generated signals carry subsurface information in the form of a temperature depth integral. Pulsed-laser PTR (PPTR) has been used in biomedical applications, especially with turbid media such as tissue.[3–6] In earlier studies,[4,5] PPTR was used as a method for determining optical properties of turbid media by using a one-dimensional (1-D) optical diffusion/thermal transfer formalism. However, the temporal decay of the thermal pulse constitutes the single signal channel available to PPTR. As a result, it was noted that a numerical fit of the radiometric theory to the data is unable to produce a unique triplet of measured values (μ_a, μ_s', K), where μ_a is the optical absorption coefficient at the exciting wavelength; μ_s' is the reduced scattering coefficient: $\mu_s' = \mu_s(1 - g)$, where μ_s is the scattering coefficient and g is the average cosine of the scattering angle, which describes the scattering anisotropy away from the forward direction; and K is a scaling parameter representing a system calibration constant.[5]

In this work, FD-PTR is introduced as an improved method for determining the absorption and scattering coefficients of turbid samples with a three-dimensional (3-D) photon diffusion model coupled to a 3-D thermal wave model. While the photon field is probably not diffuse everywhere in such low-to-intermediate-albedo phantoms, it is not exclusively described as such: The inclusion of the collimated (coherent) photon density, with its coefficients properly matched to the diffuse solution, provides a reasonable accuracy improvement for this troublesome intermediate-albedo regime. This, in turn, improves the computational accuracy greatly. It is shown that the availability of two independent signal channels (amplitude and phase), along with a least-squares multiparameter-fitting algorithm over the entire frequency-scan range, provides sufficient information to yield quantitative decoupled measurements of the coefficients μ_a, μ_s, g, and $\bar{\mu}_{\mathrm{IR}}$. Here $\bar{\mu}_{\mathrm{IR}}$ is the mean value of the infrared absorption/emission coefficient integrated over the detection bandwidth of the infrared HgCdTe sensor. The investigated samples were turbid phantoms.

2. THEORETICAL MODEL

The geometry of the system is shown in Fig. 1. The diffuse photon density $\Psi_d(\mathbf{r}, \omega)$ with an incident collimated Gaussian laser beam satisfies the diffusion equation[7,8]

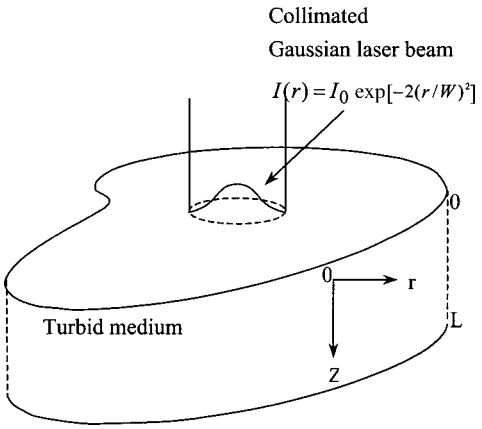

Fig. 1. Schematic of a 3-D turbid medium excited optically by a collimated Gaussian laser beam of spot size W.

$$\nabla^2\Psi_d(\mathbf{r};\omega) - \mu_{\text{eff}}^2\Psi_d(\mathbf{r};\omega) = -3\mu_s(\mu_t + g\mu_a)I(\mathbf{r})\exp(-\mu_t z), \tag{1a}$$

where the attenuation coefficient μ_t is defined as

$$\mu_t = \mu_a + \mu_s. \tag{1b}$$

Equation (1a) itself is the diffusion approximation to electromagnetic wave transport in turbid media, in the regime of multiple scattering, such that $\lambda \ll l \ll L$, where λ is the wavelength of light, $l = 1/\mu_t$ is the mean free path for photon scattering, and L is the thickness of the medium.[9] In this (macroscopic) approximation, the multiply scattered intensity is described by means of the foregoing diffusion equation. At very low modulation frequencies compared with the inverse of the diffuse-photon absorption time constant $\tau_a = 1/c\mu_a$ (c: speed of light in the medium), the complex photon wave number becomes real and is given by[10]

$$\mu_{\text{eff}} = \sqrt{3\mu_a\mu_{tr}}, \quad \mu_{tr} \equiv \mu_a + \mu_s'. \tag{2}$$

Equation (1a) is the dc limit of the diffuse-photon-density-wave equation, with synchronous time dependence of the harmonically modulated photon-density field given as

$$\Psi_d(\mathbf{r};\omega) = \Psi_d(\mathbf{r})\exp(i\omega t). \tag{3}$$

With a modulated Gaussian beam incident normal to the surface, the incident irradiance is

$$I(\mathbf{r}) = \frac{P(1-R)}{\pi W^2}\exp[-(2r^2/W^2) + i\omega t], \tag{4}$$

where P is the incident optical power, R is the specular reflection coefficient, W is the beam $1/e^2$ diameter, and $r^2 = x^2 + y^2$. The boundary conditions for the diffusion approximation are nontrivial, because near the boundaries of a turbid medium this approximation breaks down as the distance to the boundary becomes on the order of a photon mean free path. In this spatial regime, diffusive transport crosses over to free propagation (ballistic photons). Much theoretical consideration has been given to this so-called "skin layer."[11,12] Nevertheless, in keeping with the phenomenological character of the diffusion approximation, optical energy conservation principles at the turbid medium interfaces [Fig. 1] lead to the following boundary conditions[13]:

$$\Psi_d(r,0;\psi) - A\frac{\partial}{\partial z}\Psi_d(r,z;\omega)\bigg|_{z=0} = -3\mu_s g A I(r), \tag{5a}$$

$$\Psi_d(r,L;\omega) + A\frac{\partial}{\partial z}\Psi_d(r,z;\omega)\bigg|_{z=L} = 3\mu_s g A I(r)\exp(-\mu_t L), \tag{5b}$$

with

$$A \equiv 2D\left(\frac{1+r_{21}}{1-r_{21}}\right), \qquad D = \frac{1}{3\mu_{tr}}, \tag{6}$$

where r_{12} is the internal reflectance, defined as the ratio of the upward-to-downward hemispherical diffuse optical fluxes at the boundary.[14] This definition of A (in the normalized form $A \to A/2D$) has been used by Groenhuis *et al.*[15] and subsequently by Farrell *et al.*,[16] along with an empirical relationship between r_{21} and the relative refractive index n_{21}. D is the optical diffusion coefficient. The coherent photon density in the turbid medium[17] must be added to the diffuse-photon field[7]

$$\Psi_c(r,z;\omega) = [P(1-R)/\pi W^2]\exp(-2r^2/W^2 - \mu_t z) \tag{7}$$

to yield the total photon field inside the turbid medium:

$$\Psi_t(r,z;\omega) = \Psi_d(r,z;\omega) + \Psi_c(r,z;\omega). \tag{8}$$

Taking advantage of the cylindrical symmetry of the exciting Gaussian laser beam, we use the Hankel transform (λ is the Hankel variable[10]) to simplify the algebraic manipulations:

$$\tilde{\Psi}_t(\lambda,z;\omega) = \int_0^\infty \Psi_t(r,z;\omega)J_0(\lambda r)r\,dr, \tag{9}$$

where J_0 is the Bessel function of the first kind of order zero. The Hankel transform of the total photon field is

$$\tilde{\Psi}_t(\lambda,z;\omega) = \tilde{\Psi}_c(\lambda,z;\omega) + \tilde{\Psi}_d(\lambda,z;\omega) = \frac{[F_1 - \gamma F_2\exp(-\beta L)]\exp(-\beta z) + [F_2 - \gamma F_1\exp(-\beta L)]\exp[-\beta(L-z)]}{(1+A\beta)[1-\gamma^2\exp(-2\beta L)]} + \left[1 - \frac{1}{D}\left(\frac{\mu_t + g\mu_a}{\mu_t - g\mu_s}\right)\left(\frac{\mu_s}{\mu_t^2 - \beta^2}\right)\right]\exp(-\mu_t z)\tilde{I}(\lambda,\omega), \tag{10a}$$

where $\tilde{I}(\lambda,\omega)$ is the Hankel transform of the (arbitrary) radial optical source distribution $I(r,\omega)$. In this expres-

sion, the interfacial diffuse-photon transfer coefficient γ across the surface plane of the turbid medium has been defined as

$$\gamma \equiv \frac{1 - A\beta}{1 + A\beta}, \qquad \beta^2(\lambda) \equiv \lambda^2 + (\mu_a/D). \tag{10b}$$

Furthermore, the following definitions have been made:

$$F_1 = \left[3\frac{1}{D}\left(\frac{1 + \mu_t A}{\mu_t^2 - \beta^2}\right)\left(\frac{\mu_t + g\mu_a}{\mu_t - g\mu_s}\right) - \frac{2g}{\mu_{tr}}\right] \times \mu_s \tilde{I}(\lambda, \omega), \tag{11a}$$

$$F_2 = \left[3\frac{1}{D}\left(\frac{1 - \mu_t A}{\mu_t^2 - \beta^2}\right)\left(\frac{\mu_t + g\mu_a}{\mu_t - g\mu_s}\right) + \frac{2g}{\mu_{tr}}\right] \times \mu_s \exp(-\mu_t L)\tilde{I}(\lambda, \omega). \tag{11b}$$

In the absence of scattering particles in the medium, we set $\mu_s = 0$. This yields $F_1 = F_2 = 0$ in Eqs. (11) and $\mu_t = \mu_a$ in Eq. (1b). A thermal-wave source is now created in the presence of the foregoing photon field (diffuse + coherent), $\Psi_t(r, z; \omega)$, at point $\mathbf{r} = (r, z)$ in the isotropically scattering turbid medium, as a result of nonradiative deexcitation of the medium following optical absorption:[17]

$$Q(r, z; \omega) = \eta_{NR}\mu_a\Psi_t(r, z; \omega), \tag{12}$$

where Q is the thermal power density per unit volume of the medium, $\eta_{NR}\mu_a$ is the probability of one-photon loss nonradiatively per unit depth as a result of absorption, and η_{NR} is the nonradiative quantum efficiency of the optical-to-thermal energy conversion (deexcitation) process, which follows optical absorption. The thermal-wave equation can be written by using $Q(r, z; \omega)$ as the source term[17]:

$$\nabla^2 T(\mathbf{r}; \omega) - \sigma_t^2 T(\mathbf{r}; \omega) = -Q(r, z; \omega)/k, \tag{13a}$$

with

$$\sigma_t = \sqrt{i\omega/\alpha} \tag{13b}$$

being the complex thermal wave number. k is the thermal conductivity, and α is the thermal diffusivity. Again, we use the Hankel transform for convenience:

$$\tilde{T}(\lambda, z; \omega) = \int_0^\infty T(r, z; \omega) J_0(\lambda r) r \, dr. \tag{14}$$

After considerable algebraic manipulation, the final expression for the Hankel transform $T(\lambda, z; \omega)$ of the depth-dependent thermal-wave field $T(r, z; \omega)$ is[17]

$$\begin{aligned}\tilde{T}(\lambda, z; \omega) = {} & B_1\left[\exp(-\beta z) + \left[\frac{k_t\beta - h}{1 - \exp(-2qL)}\right] \times \left(\frac{1}{h + k_t q}\{\exp[-(\beta + q)L] - \exp(-2qL)\}\exp(qz) + \frac{1}{h - k_t q} \times \{1 - \exp[-(\beta + q)L]\}\exp(-qz)\right)\right] \\ & + B_2\left[\exp(\beta z) - \left[\frac{k_t\beta + h}{1 - \exp(-2qL)}\right] \times \left(\frac{1}{h + k_t q}\{\exp[-(q - \beta)L] - \exp(-2qL)\}\exp(qz) + \frac{1}{h - k_t q} \times \{1 - \exp[-(q - \beta)L]\}\exp(-qz)\right)\right] \\ & + B_3\left[\exp(-\mu_t z) + \left[\frac{k_t\mu_t - h}{1 - \exp(-2qL)}\right] \times \left(\frac{1}{h + k_t q}\{\exp[-(\mu_t + q)L] - \exp(-2qL)\}\exp(qz) + \frac{1}{h - k_t q} \times \{1 - \exp[-(\mu_t + q)L]\}\exp(-qz)\right)\right],\end{aligned} \tag{15}$$

with the following definitions:

$$B_1(\lambda, \omega) = \frac{\eta_{NR}\mu_a}{k_t(\beta^2 - q^2)} b_1(\lambda, \omega), \tag{16a}$$

$$B_2(\lambda, \omega) = -\frac{\eta_{NR}\mu_a}{k_t(\beta^2 - q^2)} b_2(\lambda, \omega), \tag{16b}$$

$$B_3(\lambda, \omega) = -\frac{\eta_{NR}\mu_a}{k_t(\mu_t^2 - q^2)} b_3(\lambda, \omega), \tag{16c}$$

with

$$b_1(\lambda, \omega) \equiv \frac{1}{H(\lambda, \omega)}[-F_1 + \gamma F_2 \exp(-\beta L)], \quad (17a)$$

$$b_2(\lambda, \omega) \equiv \frac{1}{H(\lambda, \omega)}[F_2 - \gamma F_1 \exp(-\beta L)]\exp(-\beta L), \quad (17b)$$

$$b_3(\lambda, \omega) \equiv \left[1 - \frac{\mu_s}{D(\mu_t^2 - \beta^2)}\left(\frac{\mu_t + g\mu_a}{\mu_t - g\mu_s}\right)\right]\tilde{I}(\lambda, \omega), \quad (17c)$$

$$H(\lambda, \omega) \equiv (1 + A\beta)[1 - \gamma^2 \exp(-2\beta L)]. \quad (17d)$$

In Eq. (15), h is the interfacial heat transfer coefficient. Depending on the value of h, the two limiting cases of Eq. (15) for $h = 0$ (adiabatic boundaries) and $h \to \infty$ (diathermal or isothermal boundaries) are obtained immediately. Usually, the adiabatic [homogeneous Neumann (flux)] boundary conditions are adopted for simplicity, since the temperature rise is too low in the interface region to introduce convective heat losses and the surrounding medium usually consists of a gas (air) with poor thermal properties, resulting in a small thermal coupling coefficient (the ratio of the thermal effusivities of the two media).[10] Finally, the PTR signal can then be written as[17]

$$S(r, \omega) = C\bar{\mu}_{IR}\int_0^L T(r, z; \omega)\exp(-\bar{\mu}_{IR}z)\mathrm{d}z, \quad (18)$$

where C is a constant independent of $\mathbf{r}$, and $\bar{\mu}_{IR}$, the mean infrared absorption/emission coefficient of the turbid medium, is assumed to be independent of emission wavelength. Majaron *et al.*[18] have shown that temperatures estimated from PPTR signals from turbid tissue can be in error up to 30% if the proper spectral dependence of $\bar{\mu}_{IR}(\lambda)$ is not taken into account. Nevertheless, in FD-PTR an effective (mean) value of $\bar{\mu}_{IR}$ can be extracted over all material depths from a multiparameter fit of the entire frequency-response curve (amplitude and phase) of the turbid medium. It can be shown[17] that the Hankel transform of the PTR signal [Eq. (18)] may be written as

$$\tilde{U}(\lambda, \omega) = C\bar{\mu}_{IR}\int_0^L \tilde{T}(\lambda, z; \omega)\exp(-\bar{\mu}_{IR}z)\mathrm{d}z. \quad (19)$$

Using Eq. (15), we finally obtain the complex Hankel transform

$$\begin{aligned}\tilde{U}(\lambda, \omega) = C\bar{\mu}_{IR}\Bigg\{ & B_1\Bigg[\frac{1 - \exp[-(\beta + \bar{\mu}_{IR})L]}{\beta + \bar{\mu}_{IR}} + \left[\frac{k_t\beta - h}{1 - \exp(-2qL)}\right] \\ & \times \left(\frac{1 - \exp[-(\bar{\mu}_{IR} - q)L]}{(h + k_t q)(\bar{\mu}_{IR} - q)}\{\exp[-(\beta + q)L] - \exp(-2qL)\} + \frac{1 - \exp[-(\bar{\mu}_{IR} + q)L]}{(h - k_t q)(\bar{\mu}_{IR} + q)} \times \{1 - \exp[-(\beta + q)L]\}\right)\Bigg] \\ & + B_2\Bigg[\frac{1 - \exp[-(\bar{\mu}_{IR} - \beta)L]}{\bar{\mu}_{IR} - \beta} - \left[\frac{k_t\beta + h}{1 - \exp(-2qL)}\right] \\ & \times \left(\frac{1 - \exp[-(\bar{\mu}_{IR} - q)L]}{(h + k_t q)(\bar{\mu}_{IR} - q)}\{\exp[-(q - \beta)L] - \exp(-2qL)\} + \frac{1 - \exp[-(\bar{\mu}_{IR} + q)L]}{(h - k_t q)(\bar{\mu}_{IR} + q)} \times \{1 - \exp[-(q - \beta)L]\}\right)\Bigg] \\ & + B_3\Bigg[\frac{1 - \exp[-(\bar{\mu}_{IR} + \mu_t)L]}{\bar{\mu}_{IR} + \mu_t} + \left[\frac{k_t\mu_t - h}{1 - \exp(-2qL)}\right] \\ & \times \left(\frac{1 - \exp[-(\bar{\mu}_{IR} - q)L]}{(h + k_t q)(\bar{\mu}_{IR} - q)}\{\exp[-(\mu_t + q)L] - \exp(-2qL)\} + \frac{1 - \exp[-(\mu_{IR} + q)L]}{(h - k_t q)(\bar{\mu}_{IR} + q)} \times \{1 - \exp[-(\mu_t + q)L]\}\right)\Bigg]\Bigg\}, \end{aligned} \quad (20)$$

$$q^2(\lambda, \omega) \equiv \lambda^2 + \sigma_t^2(\omega), \quad (21)$$

where F_1 and F_2 are defined in Eqs. (11a) and (11b), respectively, and γ is defined in Eqs. (10b).

3. SAMPLE PREPARATION

The turbid phantoms for the photothermal measurements were constructed by using a two-part epoxy resin as a base (MY753 resin with XD716 hardener, Ciba-Geigy Ltd), Sudan III dye as an absorber (S4131, Sigma Chemicals), and amorphous silica microspheres as scatterers (Monospher 1000M, Merck Ltd). Quantitative dilutions of these three constituents yielded scattering and absorbing phantoms with controlled optical coefficients as summarized in Table 1. A high-absorption sample with no

Table 1. Results of the Multiparameter Fit for Various Phantoms, Indicating Values Independently Measured with a Spectrophotometer, Calculated with Mie Theory, and PTR Derived

Phantom Number	μ_a (cm^{-1})		μ_s (cm^{-1})		μ_s' (cm^{-1})		g		$\bar{\mu}_{IR}$ (cm^{-1})
	Meas.[a]	Derived	Calc.[b]	Derived	Calc.[b]	Derived	Calc.[b]	Derived	Derived
1	116	118 ± 1	383	318 ± 2	13.4	11.1	0.965	0.965	600 ± 8
2	58	52 ± 2	377	318 ± 5	13.2	11.1	0.965	0.965[c]	265 ± 4
3	31	29 ± 4	383	318 ± 32	13.4	11.1	0.965	0.965[c]	153 ± 7
4	117	120 ± 2	189	326 ± 8	6.6	5.2	0.965	0.984	600 ± 7
5	184	188 ± 1	189	326 ± 2	6.6	5.2	0.965	0.984[d]	1420 ± 40
6	65	60 ± 4	189	326 ± 12	6.5	5.2	0.965	0.984[d]	233 ± 7
7	236	258 ± 2	0		0		0		420 ± 6
8	459	490 ± 2	0		0		0		460 ± 6

[a] Measured with a spectrophotometer.
[b] Calculated by using Mie theory.
[c] g value assumed the same as that for phantom 1.
[d] g value assumed the same as that for phantom 4.

scatterers was also created for use in deriving the thermal diffusivity for the entire sample set. The absorbing properties were measured spectrophotometrically in a clear dye/solidified epoxy cuvette. The scattering properties were calculated by using Mie theory[19] with the following inputs: sphere diameter = 1000 nm, wavelength = 514 nm, refractive index of sphere = 1.417, refractive index of epoxy = 1.57, and relative density of sphere to epoxy = 1.8.

To make the phantoms, we prepared concentrated absorber and scatterer stocks. The absorber stock solution was made by dissolving 0.4 g of dye powder in 100-g MY753 resin with the help of an ultrasonic bath agitator, yielding a spectrophotometer measurement of the absorption coefficient equal to 710 cm^{-1}. The stock suspension of microspheres (3% by volume) was made by mixing them with the resin in a ball mill for approximately 6 h, resulting in a reduced scattering coefficient of 24.5 cm^{-1}. Suitable amounts of resin and hardener were then mixed and combined with the resin stocks of absorber and scatterer. The mixtures were poured into 3.5-cm-diam petri dishes to a depth of ~9 mm and were allowed to solidify in a fume hood for 2 days at room temperature. Measurements were performed on the top (exposed) surface.

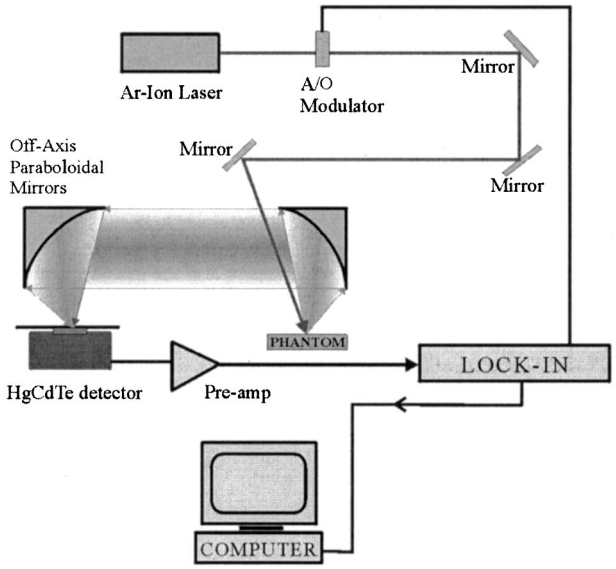

Fig. 2. Frequency-domain photothermal radiometric instrumentation.

4. EXPERIMENTAL SYSTEM

The experimental setup is shown in Fig. 2. A 514.5-nm-wavelength cw Ar^+ laser (Innova 100, Coherent Inc.) was modulated by an external acousto-optic (A/O) modulator (AOM-Isomet 1201E-1) at frequency $f = \omega/2\pi$, where ω is the angular modulation frequency. The laser beam was then focused onto a sample to a $1/e^2$ spot radius of 0.48 mm at an incident angle of ~12° off normal and at a power of 0.1 W. The blackbody radiation from the optically excited sample was collected, collimated, and focused by two paraboloidal mirrors onto a liquid-nitrogen-cooled HgCdTe detector (EG&G Judson J15D12-M204-S050U). The HgCdTe detector was a photoconductive element with a typical responsivity of 1×10^3 V/W, which undergoes a change in resistance proportional to the intensity of the incident infrared radiation. The detector had an active square size area of 1 mm × 1 mm and a spectral bandwidth of 2–12 μm. Its performance improves with decreasing temperature, so the detector was operated at a cryogenic temperature of 77 K by using liquid-nitrogen cooling. An antireflection-coated germanium window with a transmission bandwidth of 2–14 μm was mounted in front of the detector to block any visible radiation from the laser. Before being sent to the digital lock-in amplifier (Stanford Research Systems SR850), the photothermal radiometric signal was amplified by a preamplifier with a dc 1-MHz frequency bandwidth (EG&G Judson PA-300), especially designed for operation with the HgCdTe detector. The process of data acquisition, storage, and frequency scanning was under computer control. With this experimental arrangement, a dynamic experiment could be performed at one location on the sample. The experiment generated depth-dependent information by scanning the laser-intensity modulation frequency (a "frequency scan"). Two independent channels of information (amplitude and phase) were thus obtained.

5. EXPERIMENTAL RESULTS, MULTIPARAMETER COMPUTATIONS, AND DISCUSSION

Photothermal measurements were performed in the frequency domain over the 10–1000-Hz range. The inverse Hankel transform of Eq. (20) was used to fit the experimental amplitude and phase data sets. The Hankel integral is an improper integral; i.e., its upper limit is infinite. It is assumed, based on the physical quantity represented by the complex integrand, that the integral exists and approaches a finite value as the upper limit of integration approaches infinity. The integration is calculated by using the improper integral routine *qromo* with *midpnt* taken from *Numerical Recipes in C*.[20] The needed known parameters used as inputs were the $1/e^2$ beam radius $W = 0.48$ mm, the thermal conductivity of epoxy $k = 0.446$ W/m K, and the semiempirical internal reflection parameter, calculated[3] to be $r_{21} = 3.517$. The thermal diffusivity α and the effective (mean) infrared absorption coefficient $\bar{\mu}_{\mathrm{IR}}$ were determined with a least-residual analysis of the data from the high-absorption-only sample. The absorption coefficient for this reference phantom was 710 cm^{-1}. The residuals are the sums over the frequency scans of the theoretical fit minus experimental data squared, where both amplitude and phase information is used. The resultant residual contour plot is shown in Fig. 3, and the minimum determines a unique solution pair ($\bar{\mu}_{\mathrm{IR}} = 480\,\mathrm{cm}^{-1}$, $\alpha = 0.9 \times 10^{-7}\,\mathrm{m}^2/\mathrm{s}$) in the region. The solution is determined by least-residual search in the possible range of epoxy $\bar{\mu}_{\mathrm{IR}}$ and thermal diffusivity values. The major advantage of using FD-PTR as opposed to PPTR is that two channels of information (amplitude and phase) exist for fitting the data, and thus a unique two-parameter determination can be achieved.

The thermal diffusivity derived from the reference sample was then used in the analysis of all the other phantoms, and the summary of all the results is shown in Table 1. The "measured values" for μ_a are based on the spectrophotometer measurements. The "calculated values" for μ_s' are the results of Mie-theory calculations. The "derived values" are the optimal fitted parameter sets with the use of Eq. (20). The uncertainty for each fitting parameter was found by evaluating an arbitrarily chosen 5% residual change on the theoretical fit. For the nonscattering samples, phantoms 7 and 8, two-dimensional contour plots (μ_a, $\bar{\mu}_{\mathrm{IR}}$) were used to find the minimum solutions of unique pairs of the optical absorption (μ_a) and mean infrared absorption ($\bar{\mu}_{\mathrm{IR}}$) coefficients. The results are also shown in Table 1. It is observed that the mean infrared absorption coefficient increases with increasing optical absorption at 514 nm. This is possibly an artifact of the constancy of μ_{IR} in Eq. (20), since higher μ_a would result in collection of IR photons closer to the sample surface, thus increasing the effective collection solid angle. This would be attributed to an increase in the effective $\bar{\mu}_{\mathrm{IR}}$ of the measurement during the multiparameter fit. For the scattering samples, the fitted parameters were (μ_a, $\bar{\mu}_{\mathrm{IR}}$, μ_s, g): the optical absorption, the mean infrared absorption coefficient, the scattering coefficient, and the average cosine of the scattering angle, respectively. In tissue the value of g lies in the 0.6–0.98 range.[21] Starting with the $g = 0.965$ value for the first scattering sample (phantom 1), which was calculated by using Mie theory,[19] a 3-D contour plot as shown in Fig. 4(a) resulted in the minimum triplet solution of parameters μ_a, $\bar{\mu}_{\mathrm{IR}}$, and μ_s. The 3-D contour is shown for three $\bar{\mu}_{\mathrm{IR}}$ values of

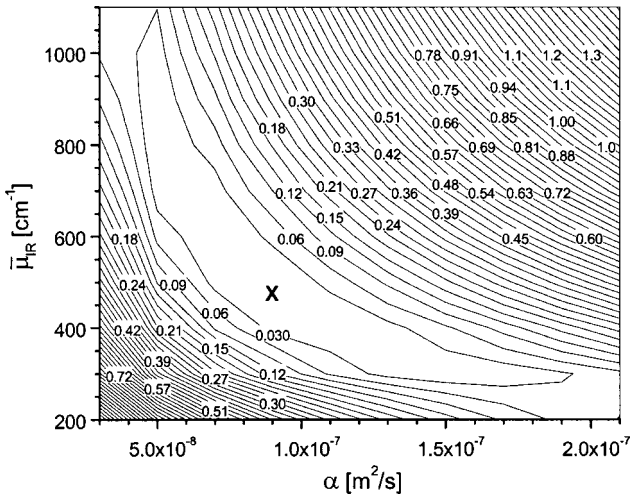

Fig. 3. Least-residual contour surface for reference medium with high absorption and no scatters (stock b). A local minimum marked by "×" yields the optimum ($\bar{\mu}_{\mathrm{IR}} = 480\,\mathrm{cm}^{-1}$, $\alpha = 0.9 \times 10^{-7}\,\mathrm{m}^2/\mathrm{s}$) pair. This number indicates the best solution to fit the experimental data in stock b.

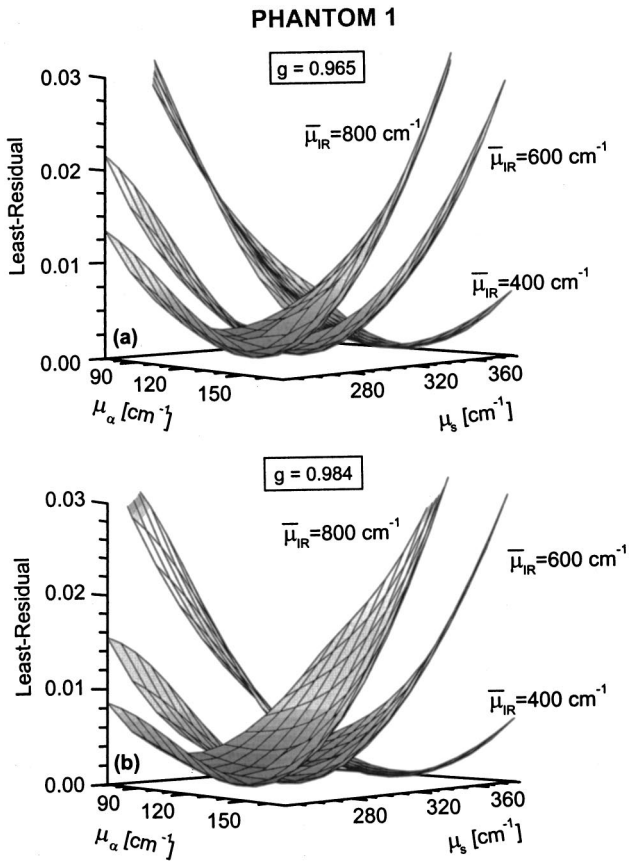

Fig. 4. 3-D contour plot for phantom 1: (a) $g = 0.965$ and (b) $g = 0.984$. The minimum set of values obtained for $g = 0.965$ is ($\mu_a = 118\,\mathrm{cm}^{-1}$, $\bar{\mu}_{\mathrm{IR}} = 600\,\mathrm{cm}^{-1}$, $\mu_s = 318\,\mathrm{cm}^{-1}$) and for $g = 0.984$ is ($\mu_a = 118\,\mathrm{cm}^{-1}$, $\bar{\mu}_{\mathrm{IR}} = 600\,\mathrm{cm}^{-1}$, $\mu_s = 303\,\mathrm{cm}^{-1}$).

400, 600, and 800 cm^{-1}, and although graphically difficult to see, the minimum is obtained at $\bar{\mu}_{IR} = 600\,cm^{-1}$. To further generalize the optimization method, we repeated the procedure for creating the 3-D contour for several higher and lower g values. Figure 4(b) shows a 3-D contour for another (arbitrary) $g = 0.984$. Calculating minima for several g values including the ones shown in Fig. 4, we found that the absolute triplet minimum is obtained for $g = 0.965$ within the domain of (μ_a, μ_s) values indicated in Fig. 4(a). The best fit to the PTR amplitude and phase of phantom 1 data corresponding to this triplet is shown in Fig. 5. The same g value as that for phantom 1 was then used for the samples with the same scattering coefficient, phantoms 2 and 3, and 3-D contours were constructed, with the results presented in Table 1. It is again observed that as μ_a increases, the effective mean $\bar{\mu}_{IR}$ increases within this group of samples with similar scattering properties. For phantoms with different scattering coefficients, 3-D contours similar to those in Fig. 4 with several g values were again constructed. In the same manner, the 3-D contour plot was used to determine the minimum solution parameter set $(\mu_a, \mu_s, \bar{\mu}_{IR})$. From comparison of several g values, it was found that the absolute minimum within the domain of (μ_a, μ_s) values now occurs for $g = 0.984$. The contours for the Mie-theoretical value $g = 0.965$, which were used as a starting point for the search, and those obtained for the derived absolute minimum value $g = 0.984$ are shown in Figs. 6(a) and 6(b), respectively. The best fit to the data corresponding to this triplet for phantom 4 is shown in

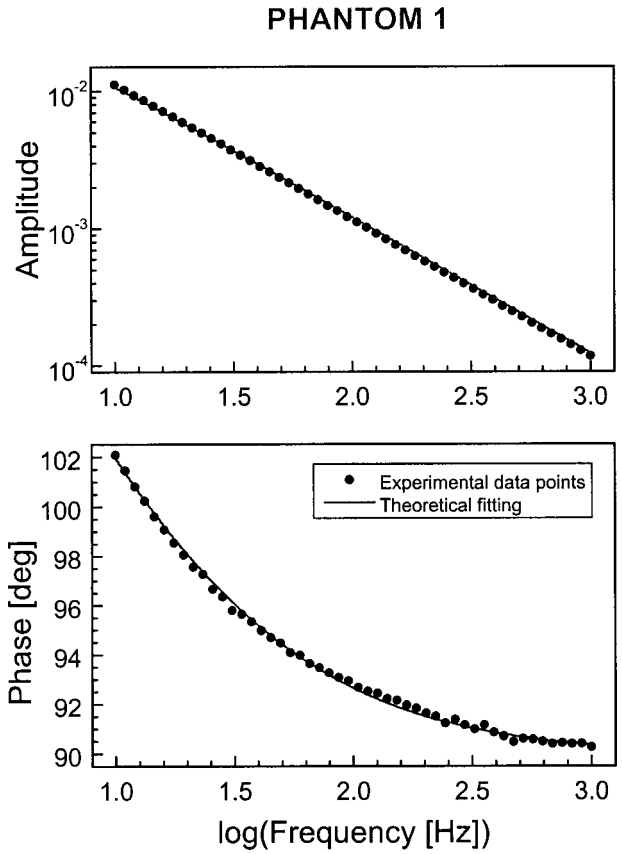

Fig. 5. Amplitude and phase fits for phantom 1 from the minimum solution obtained by the 3-D contour in Fig. 4(a).

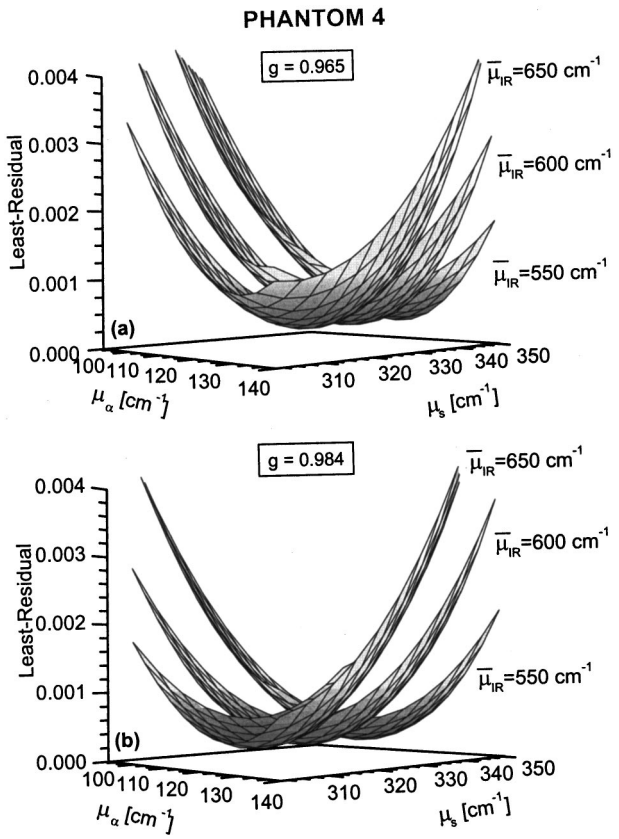

Fig. 6. 3-D contour plot for phantom 4: (a) $g = 0.965$ and (b) $g = 0.984$. The minimum set of values obtained for $g = 0.965$ is $(\mu_a = 116\,cm^{-1}, \bar{\mu}_{IR} = 600\,cm^{-1}, \mu_s = 351\,cm^{-1})$ and for $g = 0.984$ is $(\mu_a = 120\,cm^{-1}, \bar{\mu}_{IR} = 600\,cm^{-1}, \mu_s = 326\,cm^{-1})$.

Fig. 7. The g value thus determined from phantom 4 was then kept constant for the set of samples with the same scattering coefficient, and further 3-D contours were constructed, with the results reported in Table 1.

Just as in the case of the scattering group of phantoms 1–3, it is observed that, within the group of scattering samples 4–6, the effective mean infrared absorption coefficient exhibits changes similar to those of the absorption coefficient at 514 nm. The $\bar{\mu}_{IR}$ coefficients for the absorption-only samples 7 and 8 also decrease with decreasing μ_a, although their variation is considerably less than that of the scattering samples. This suggests that scattering affects more strongly the value of the effective $\bar{\mu}_{IR}$, as is expected, since it may control the optical penetration depth and the lateral loss of photons outside the (very narrow) solid angle subtended by the active HgCdTe detector element. Furthermore, among the scattering samples, as μ_s decreases, the average cosine of the scattering angle, g, increases. This trend is also expected, since lower μ_s results in a more forward-scattered photon distribution with a smaller scattering angle θ and, therefore, a larger mean cosine of the scattering function.[21]

From the results of Table 1, it is seen that the optical absorption coefficients μ_a of all phantoms are estimated quite accurately by means of PTR multiparameter fits. All derived values, however, for the reduced scattering coefficients μ_s' are lower than the ones calculated by using Mie theory. This is depicted graphically in Fig. 8, where

the percent deviations from the actual values for both absorption and reduced scattering coefficients are shown. A possible cause of the larger scattering coefficient discrepancy is the use of Mie theory to independently calculate the scattering coefficient. From Fig. 8, it can be seen that the deviation in reduced scattering coefficient decreases somewhat as the measured scattering coefficient increases. Unfortunately, there appear to be no literature data for μ_s with which one may compare the present derived values, because earlier 1-D models[3–6] of the diffuse-photon density in turbid media involved the reduced scattering coefficient μ_s' and not its constituent parameters μ_s and g separately. Overall, the theoretical model used in this work[17] seems to be sufficient for determining the optical properties of turbid samples in the examined (μ_a, μ_s') range. The results are underdetermined by 20% for μ_s' and have variations up to 10% for μ_a. The larger apparent discrepancy between calculated and derived μ_s values for phantoms 4–6 in Table 1 cannot be easily accounted for in physical terms. It is believed that it originates in the (unfortunately nonmeasurable) computational uncertainty in the g values, which produce the absolute minima in Figs. 4 and 6, $g = \min[g(\mu_a, \mu_s)]$. Owing to the structure if the defining equation $\mu_s = \mu_s'/(1 - g)$, for a derived value of μ_s and for g values near unity, e.g., for $g = 0.984$, a 1% variation in g causes μ_s variations up to 65%. Therefore the actual standard deviation in the derived μ_s values in Table 1 can be much higher than the apparent standard deviations if a small nonzero uncertainty is allowed for the value of g.

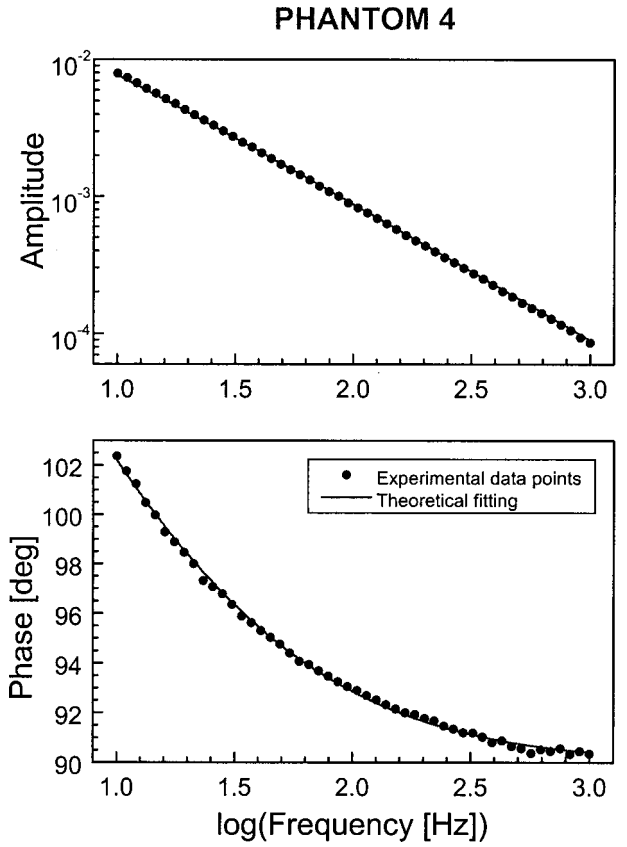

Fig. 7. Amplitude and phase fits for phantom 4 from the minimum solution obtained by the 3-D contour in Fig. 4(b).

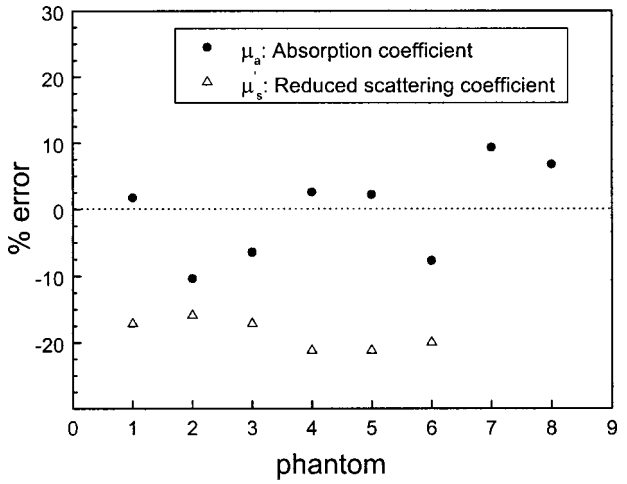

Fig. 8. Percent deviation (from independently derived values) of μ_a and μ_s' as determined from the 3-D FD-PTR analysis.

6. CONCLUSIONS

A complete FD-PTR theoretical, experimental, and computational multiparameter methodology for measuring optical properties of turbid media has been introduced. A new theoretical FD-PTR signal model based on a 3-D expression of the total (diffuse + coherent) photon density field at very low modulation frequencies (with respect to optical transport rates) has been used. The model accounts rigorously for full 3-D optical diffusion as a volume source to a 3-D thermal-wave model. Complete amplitude and phase scans were obtained for all test phantoms as functions of frequency. The theoretical expressions were utilized in the quantitative analysis of the experimental data. The enhanced signal-to-noise ratio of the FD-PTR lock-in amplifier demodulated signals, compared with PPTR transients, and the availability of two information channels (amplitude and phase), instead of a single-channel transient decay, are distinct advantages of FD-PTR.[22] The methodology shows good promise with regard to its analytical ability to measure triplets of $(\mu_a, \bar{\mu}_{IR}, \mu_s')$ values of turbid media *uniquely*, as compared with its pulsed counterpart, which exhibits uniqueness problems, thus requiring the use of independent measurements.[5] In the data sets examined in this work, the PTR-derived optical reduced scattering and absorption coefficients were found to be within 20% and 10%, respectively, of the values independently derived by using Mie theory and spectrophotometric measurements.

ACKNOWLEDGMENTS

The support of Materials and Manufacturing Ontario and the Natural Science and Engineering Research Council is gratefully acknowledged.

Address correspondence to Andreas Mandelis at the location on the title page or by e-mail, mandelis@mie.utoronto.ca.

REFERENCES

1. M. Munidasa, T. C. Ma, A. Mandelis, S. K. Brown, and L. Mannik, "Non-destructive depth profiling of laser processed Zr-2.5Nb alloy by infrared photothermal radiometry," J. Mater. Sci. Eng. A **159**, 111–118 (1992).
2. G. Busse and H. G. Walther, "Photothermal nondestructive evaluation of materials with thermal waves," in *Progress in Photothermal and Photoacoustic Science and Technology*, A. Mandelis, ed. (Elsevier, New York, 1992), Vol. 1, pp. 205–298.
3. R. R. Anderson, H. Beck, U. Bruggemann, W. Farinelli, S. L. Jacques, and J. A. Parrish, "Pulsed photothermal radiometry in turbid media: internal reflection of backscattered radiation strongly influences optical dosimetry," Appl. Opt. **28**, 2256–2262 (1989).
4. I. A. Vitkin, B. C. Wilson, and R. R. Anderson, "Pulsed photothermal radiometry applications in biological media," in *Optical-Thermal Response of Laser-Irradiated Tissue*, A. J. Welch and M. J. C. van Gemert, eds. (Plenum, New York, 1995), Chap. 16.
5. S. A. Prahl, I. A. Vitkin, U. Bruggemann, B. C. Wilson, and R. R. Anderson, "Determination of optical properties of turbid media using pulsed photothermal radiometry," Phys. Med. Biol. **37**, 1203–1217 (1992).
6. F. H. Long, R. R. Anderson, and T. F. Deutsch, "Pulsed photothermal radiometry for depth profiling of layered media," Appl. Phys. Lett. **51**, 2076–2078 (1987).
7. A. Ishimaru, Y. Kuga, R. L-T. Cheung, and K. Shimizu, "Scattering and diffusion of a beam wave in randomly distributed scatterers," J. Opt. Soc. Am. **73**, 131–136 (1983).
8. A. Mandelis, "Diffusion waves and their uses," Phys. Today **53**, 29–34 (2000).
9. E. Amic, J. M. Luck, and Th. M. Nieuwenhuizen, "Multiple Rayleigh scattering of electromagnetic waves," J. Phys. (Paris) I **7**, 445–483 (1997).
10. A. Mandelis, *Diffusion-Wave Fields: Mathematical Methods and Green Functions* (Springer-Verlag, New York, 2001), Chap. 10.
11. Th. M. Nieuwenhuizen and J. M. Luck, "Skin layer of diffusive media," Phys. Rev. E **48**, 569–588 (1993).
12. M. C. W. van Rossum and Th. M. Nieuwenhuizen, "Multiple scattering of classical waves: microscopy, mesoscopy and diffusion," Rev. Mod. Phys. **71**, 313–370 (1999).
13. A. Ishimaru, *Wave Propagation and Scattering in Random Media* (Academic, New York, 1978), Chap. 9.
14. Ref. 3, p. 2261, Eq. (8).
15. R. A. J. Groenhuis, H. A. Ferwerda, and J. J. Ten Bosch, "Scattering and absorption of turbid materials determined from reflection measurements. 1: Theory," Appl. Opt. **22**, 2456–2462 (1983).
16. T. J. Farrell, M. S. Patterson, and B. Wilson, "A diffusion theory model of spatially resolved, steady-state diffuse reflectance for the noninvasive determination of tissue optical properties in vivo," Med. Phys. **19**, 879–888 (1992).
17. A. Mandelis and C. Feng, "Theory of frequency-domain infrared radiometric detection of diffuse-photon-density- and photothermal waves in turbid media" (manuscript available from A. Mandelis, mandelis@mie.utoronto.ca).
18. B. Majaron, W. Verkruysse, B. S. Tanenbaum, T. E. Milner, and J. S. Nelson, "Pulsed photothermal profiling of hypervascular lesions: some recent advances," in *Lasers in Surgery: Advanced Characterization, Therapeutics and Systems X*, R. R. Anderson, K. E. Bartels, L. S. Bass, C. G. Garrett, K. W. Gregory, N. Kollias, H. Lui, R. S. Malek, G. M. Peavy, H.-D. Reidenbach, L. Reinisch, D. S. Robinson, L. P. Tate, Jr., E. A. Towers, and T. A. Woodward, eds., Proc. SPIE **3907**, 114–125 (2000).
19. C. F. Bohren and D. R. Huffman, *Absorption and Scattering of Light by Small Particles* (Wiley, New York, 1983), Appendix A.
20. W. H. Press, S. A. Teukolsky, W. T. Vetterling, and B. P. Flannery, *Numerical Recipes in C*, 2nd ed. (Cambridge U. Press, New York, 1992).
21. W. M. Star and J. P. A. Marijnissen, "New trends in photobiology light dosimetry: status and prospects," J. Photochem. Photobiol. B **1**, 149–159 (1987).
22. A. Mandelis, "Signal-to-noise ratios in lock-in amplifier synchronous detection: a generalized communications systems approach with applications to frequency-, time- and hybrid (rate-window) photothermal measurements," Rev. Sci. Instrum. **65**, 3309–3323 (1994).